Analysis of Stator Slots and Rotor Pole Pairs Combinations of Rotor-Permanent Magnet Flux-Switching Machines

Peng Su, *Student Member*, *IEEE*, Wei Hua, *Senior Member*, *IEEE*, Mingjin Hu, Zhongze Wu, *Member*, *IEEE*, Jikai Si, Zhe Chen, *Fellow*, *IEEE*, Ming Cheng, *Fellow*, *IEEE*

Abstract—Abstract—This paper investigates the influence of stator slots and rotor pole pairs combinations on torque performances in rotor permanent magnet flux switching machines. Based on a magnetomotive force permeance model, the candidates of stator slots and rotor pole pairs combinations with higher torque capability can be determined by analysing the permanent magnet magnetomotive force and winding factor. Meanwhile, the candidates with a lower torque ripple can be obtained by referring to the cogging torque, which is related to the greatest common divisor of stator slots and rotor pole pairs. In addition, from the field modulation principle, the rotor-permanent magnet flux-switching machines with the same fundamental magnetic loadings and winding factors exhibit identical fundamental harmonic toque, but different modulation harmonic components. Finally, four candidates with attractive torque performance are chosen, and the characteristics are verified by finite element analysis and experiments.

Index Terms—Analytical models, finite element analysis, flux switching, permanent magnet machines, rotors, slots and pole pairs combination, torque.

Manuscript received Aug. 20, 2018; revised Nov. 14, 2018 and Jan. 12, 2019; accepted Feb. 9, 2019. This work was supported in part by the Changjiang Scholars Program of China under Grant Q2017110. (*Corresponding author: Wei Hua.*)

Peng Su, Wei Hua, Mingjin Hu and Ming Cheng are with the School of Electrical Engineering, Southeast University, Nanjing, 210096 China, (e-mail: supeng1639@126.com, huawei1978@seu.edu.cn, 1205195957@qq.com and mcheng@seu.edu.cn).

Zhongze Wu is with Department of Mechanical Engineering, University of Bath, Bath BA2 7AY, U.K. (e-mail: z.wu@bath.ac.uk).

Jikai Si is with the Department of Electrical Engineering, Zhengzhou University, Zhengzhou 450006, China (e-mail: sijikai527@126.com)

Zhe Chen is with the Department of Energy Technology, Aalborg University, Aalborg 9220, Denmark (e-mail: zch@et.aau.dk).

Nomenclature

B_{gv}	Magnetic loading of *v*-order harmonic
B_{Rw}	Modulated armature reaction flux density
D_{so},	D_{si} Outer and inner diameters
F_{Rw}	Armature reaction-MMF function
F_{RPMb}	PM-MMF amplitude
H_c	PM coercivity
I_{Rmax}	Maximum value of the phase current
J_{sa_rms}	Armature current density
K_{sv}	Electrical loading of *v*-order harmonic
L_d, L_q	*dq*-axes inductances
N_{sp}	Spoke number of conductors back EMF vectors
N_{Rc}	Coil turns number
P_s, P_r, P_{PM}	Numbers of stator slots, rotor pole pairs and PM pole pairs.

T_{cog}, T_e	Cogging torque and electromagnetic torque
T_{ef}, T_{em}	Fundamental and modulation harmonic torque components
g	Air gap length
h_{PM}	PM height
k_{fw}	Flux weakening coefficient
k_{wv}	Winding factor of v-order harmonic
l_a	Stack length
w_{PM}, w_{rt}	PM width and rotor tooth width
Λ_{gap}, Λ_{PM}	Air-gap and PM magnetic permeances
Φ_{PMg}	Air-gap PM flux linkages
β_{st}, β_{rt}, β_{rs}	Stator tooth, rotor tooth and rotor slot arcs
ω_{rv}	Rotation speed of v-order harmonic
μ_0, μ_{PM}	Air and PM relative permeabilities
ϑ_0, ϑ_r	Initial rotor position and rotation angle

1. Introduction

For electric vehicles (EVs), special characteristics are desired for the traction machines, such as large torque capability, low torque ripple, strong overload ability, and high efficiency [1], [2]. Recently, a new rotor-permanent magnet (PM) flux-switching (FS) (RPM-FS) machine was proposed, which evolves from the topology of stator-PM flux-switching (SPM-FS) machines. The RPM-FS machines not only inherit the advantages of SPM-FS machines, including high torque (power) density and efficiency [3], [4], but also improve the overload capability due to relieving the saturation level of stator teeth [5]. Hence, the RPM-FS machines can be identified as a promising candidate of traction machines in EVs.

For the flux-switching machines, the combination of stator slots number P_s and rotor pole-pairs number P_r significantly affects electromagnetic performances, which is a key parameter in the design process [6]. Generally, the feasible combinations of P_s and P_r for SPM-FS machines can be determined based on the back electro-motive-force (EMF) vectors distribution of slot conductors, and then can be chosen according to the winding factor k_w [7]-[8]. However, since the electromagnetic torque is not determined only by k_w, it is difficult to select the proper P_s/P_r combinations with higher torque capability. Hence, the torque capability of machines with different P_s/P_r are investigated further by the air-gap surface occupation factor (ASOF) [9] and pole ratio (PR) [10], which are helpful in reducing the selection range. Moreover, it is found that the combinations that satisfy $P_s=P_r\pm k$ (k=1, 2) can exhibit a higher electromagnetic torque, and they are chosen as the attractive candidates. Nevertheless, for the combinations, which are simply the integer multiples of the smallest equivalent machines with the lowest pole numbers, e.g., 12s/10p versus 6s/5p machines, the ASOF and PR between two machines are equal, i.e., ASOF=0.208 [9] and PR=2.5 [10]. Thus, it is still difficult to directly evaluate the torque capability of such combinations and choose the optimal candidates for SPM-FS machines. For RPM-FS machines, the torque performance is dramatically influenced by the P_s/P_r combinations, and the attractive combinations of P_s/P_r should also be provided at the preliminary design stage.

The purpose of this paper is to investigate the influence of P_s/P_r combinations on electromagnetic torque performances, ultimately contributing to the choice of candidates with attractive torque performances. The P_s/P_r combinations performance is investigated from three perspectives, i.e. magnetic loading, electrical loading, and cogging torque production. Based on the field modulation principle, the PM field and armature reaction field at different P_s/P_r combinations are analyzed. Meanwhile, the analytical expressions of cogging torque with different P_s/P_r combinations of RPM-FS machine are deduced in section II. Then, four RPM-FS machines 24-stator-slots/10-rotor-pole-pairs (24s/10p), 24s/11p, 24s/13p

and 24s/14p are selected as the candidates exhibiting higher torque output torque and lower torque ripple. In section III, a comprehensive electromagnetic characteristics comparison between four RPM-FS machines candidates and a typical 12s/10p SPM-FS machine with the same structure dimensions is conducted. Then the prototyped machines are manufactured and tested to verify the effectiveness of the proposed technique. It can be concluded that the RPM-FS machines candidates exhibit an attractive torque performance. Finally, conclusions are drawn in section IV.

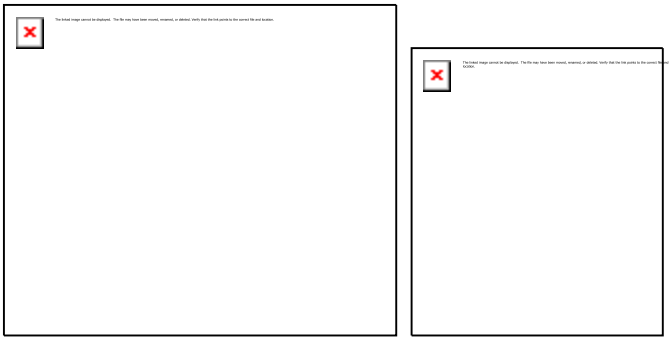

(a) (b)

Fig. 1 A three-phase 24s/10p RPM-FS machine. (a) The cross section topology. (b) The key geometric parameters.

2. Slots and Pole-Pairs Combination Principles

The topology of a 24s/10p RPM-FS machine, shown in Fig. 1, is evolved from a typical 12s/10p SPM-FS machine and inherits the flux-switching principle [5]. Based on the slot-conductor back-EMF star vectors theory, feasible combinations of the stator slots number P_s and the rotor pole pairs number P_r can be determined by the spoke number N_{sp} in Fig. 2, where N_{sp} is expressed as [7], [10], [11]:

(1)

where GCD(P_s, P_r) is the greatest common divisor of P_s and P_r.

Obviously, N_{sp} must be an integer divisible by phase number (e.g., m=3). From equation (1), the possible N_{sp} of the RPM-FS machines with P_s=24 and single-layer concentrated winding can be deduced as four cases, i.e., N_{sp}=3, 6, 12 and 24, and the corresponding GCD(P_s, P_r) values are 8, 4, 2 and 1. Therefore, the feasible combinations of P_s/P_r are listed in Table I. Similarly, the feasible P_s/P_r combinations in the cases of P_s=18, 12 and 6 are respectively listed in Tables II, III and IV.

Based on the results shown in Tables I-IV, the combinations of P_s/P_r can be selected preliminarily according to the winding factor k_w; e.g., the 12s/5p, 18s/10p, 24s/10p, 24s/11p, etc., can be adopted with higher k_w. However, for P_s/P_r combinations with the same k_w, the electromagnetic torque should be evaluated based on equation (2) [12].

(2)

where D_{si} is stator inner diameter, l_a is stack length, and φ_v is the v-order harmonic angle between magnetic loading B_{gv} and electrical loading K_{sv}. The torque of RPM-FS machines is contributed not only by the fundamental component (v=P_{PM}, where P_{PM} is the PM pole-pair number, equal to P_r in RPM-FS machines) but also by the modulation harmonics (v=|P_{PM}±P_s|) [12]. Hence, the harmonics of the winding factor k_{wv}, magnetic loading B_{gv} and electrical loading K_{sv} should be analysed for the selected combinations of P_s/P_r.

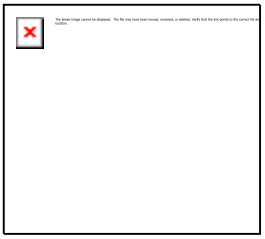

Fig. 2 The slot-conductors back-EMF vectors distribution.

Table I

Combinations of P_s=24 and P_r for RPM-FS machines

GCD(P_s, P_r)		P_s=24				
GCD=1, N_{sp}=24	P_r	1	5	7	**11**	**13**
	k_w	0.126	0.588	0.766	**0.958**	**0.958**
GCD=2, N_{sp}=12	P_r	2	**10**	**14**	22	26
	k_w	0.259	**0.966**	**0.966**	0.259	0.259

GCD=4, N_{sp}=6	P_r	4	20	28	…
	k_w	0.5	0.5	0.5	
GCD=8, N_{sp}=3	P_r	8	**16**	32	…
	k_w	0.866	**0.866**	0.866	

Table II

Combinations of P_s=18 and P_r for RPM-FS machines

GCD(P_s, P_r)		P_s=18				
GCD=1, N_{sp}=18	P_r	1	5	7	**11**	13
	k_w	0.167	0.735	0.9	**0.9**	0.735
GCD=2, N_{sp}=9	P_r	2	4	8	**10**	14
	k_w	0.328	0.617	0.945	**0.945**	0.617
GCD=3, N_{sp}=6	P_r	3	15	21	33	…
	k_w	0.5	0.5	0.5	0.5	
GCD=6, N_{sp}=3	P_r	6	**12**	24	30	…
	k_w	0.866	**0.866**	0.866	0.866	

Table III

Combinations of P_s=12 and P_r for RPM-FS machines

GCD(P_s, P_r)		P_s=12				
GCD=1, N_{sp}=12	P_r	1	5	7	11	13
	k_w	0.259	0.966	0.966	0.259	0.259
GCD=2, N_{sp}=6	P_r	2	10	14	22	26
	k_w	0.5	0.5	0.5	0.5	0.5
GCD=4, N_{sp}=3	P_r	4	8	16	20	28
	k_w	0.866	0.866	0.866	0.866	0.866

Table IV

Combinations of P_s=6 and P_r for RPM-FS machines

GCD(P_s, P_r)		P_s=6				
GCD=1, N_{sp}=6	P_r	1	5	7	11	13
	k_w	0.5	0.5	0.5	0.5	0.5
GCD=2, N_{sp}=3	P_r	2	4	8	10	14
	k_w	0.866	0.866	0.866	0.866	0.866

1. Magnetic loading

For the PM-excited field, the PM-MMF is modulated by the salient stator teeth, and then the magnetic loading $B_g(\vartheta,t)$ of a RPM-FS machine with the primitive dimensions listed in Table V can be deduced as [12]:

(3)

where F_{RPMb} is the PM-MMF amplitude; F_{RPMn} are the Fourier series coefficients of the PM-MMF distribution; n is 1, 2, 3…; Λ_{S0}, Λ_{Sb} and Λ_{Sk} are the corresponding Fourier series coefficients of stator air-gap permeance, respectively; k is 1, 2, 3…; ω_r is rotor angular speed; and ϑ_0 is the initial rotor position. It can be established from equation (3) that $B_g(\vartheta, t)$ is composed of fundamental components with nP_{PM} orders and modulation harmonic components with $|nP_{PM}\pm kP_s|$ orders. The amplitudes of the harmonic components are mainly determined by PM-MMF amplitude F_{RPMb} and stator air-gap permeance Λ_s, where the PM-MMF amplitude F_{RPMb} can be deduced by the magnetic circuit equation (4), where the permeability of the iron core is assumed to be infinite.

(4)

(5)

where H_c is PM coercivity and w_{PM} and w_{cg} are PM width and cell gap width, equal to the rotor tooth width $w_{rt}=\pi D_{si}/(4P_r)$ in the primitive design. Λ_{gap} and Λ_{PM} are the magnetic permeance of the air-gap and PM, respectively. Φ_{PMg} is the air-gap PM flux linkage. l_a is the stack length, h_{PM} is the PM height, h_{rt} is rotor teeth height, and μ_0 and μ_{PM} are the relative permeabilities of air and PMs, respectively. g is the air gap length. Then, the rotor PM-MMF F_{RPMb} in an air-gap field can be determined as follows:

(6)

Table V

The Primitive Design Parameters of RPM-FS Machines

Items	Values
Stator outer diameter D_{so} (mm)	128
Stator inner diameter D_{si} (mm)	79.36
Stack length l_a (mm)	75
Airgap length g (mm)	0.35
Stator tooth arc θ_{st} (deg.)	π/P_s
Rotor tooth arc θ_{rt} (deg.)	$\pi/(2P_r)$
Rotor slot arc θ_{rs} (deg.)	$\pi/(2P_r)$

It can be found from equation (6) that the F_{RPMb} is dominantly determined by the D_{si} and P_r. The analytically predicted characteristics of F_{RPMb} vs. P_r are compared to those from FEA, as shown in Fig. 3. The analytical F_{RPMb} increases first and then decreases when P_r=16 at D_{si}=79.36 mm, which is similar to the trend of FEA-predicted result. For D_{si}=40 mm, the highest F_{RPMb} are obtained at P_r=10 by FEA and P_r=12 by the analytical solution. The difference is attributed to the simplified MMF permeance model that ignores the iron core permeability. Overall, the variation trends from the analytical solution and FEA prediction agree well. In addition, since the PM volumes of RPM-FS machines with different P_s/P_r combinations are identical in the same D_{si}, e.g. D_{si}=79.36 mm, V_{PM}=34733 mm^3, the waveforms of $k_{MMF/VPM}$ (the ratio of PM MMF to PM volume) with different P_r coincide exactly with the waveforms of PM-MMF vs. P_r, as shown in Fig. 3.

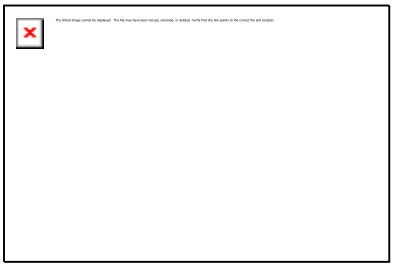

Fig. 3 The per-unit of PM-MMF amplitudes F_{RPMb} with different P_r of RPM-FS machines.

From the feasible combinations of P_s/P_r listed in Table I-IV, the influence of P_r on magnetic loading B_{gv} can be analyzed and compared in two cases, namely, the machines with the same P_s and the machines with different P_s but the same k_w.

For the RPM-FS machines with the same P_s=24, the cases of P_r=8, 10, 11, 13, 14 and 16 are analyzed due to larger k_w values in Table I. The open-circuit air-gap flux density harmonic distributions are shown in Fig. 4. It can be found that the fundamental harmonic amplitude of PM flux density B_{gv} (v=P_{PM}) is the lowest when P_r=8 (B_{g8}=0.65T), due to the minimum F_{RPMb} among 6 cases in Fig. 3. Hence, to obtain a larger B_{gv} (v=P_{PM}) under the same P_s condition, a higher P_r should be chosen based on the F_{RPMb} distribution.

On the other hand, as shown in Fig. 4(b), the fundamental harmonics B_{gv} and k_{wv} (v=P_{PM}) of the RPM-FS machines with P_r=10 and 14 are equal, i.e., B_{gv}=0.7T and k_{wv}=0.966, since the PM-MMF at P_r=10 and 14 are approximately identical. However, the corresponding modulation harmonic ($|P_{PM}$-$P_s|$) amplitudes are different, resulting in an identical fundamental component T_{ef} and different modulation harmonic torque T_{em}. The influence on electromagnetic torque T_e is analyzed further in Part D. Similarly, the RPM-FS machines with 24s/11p and 24s/13p have the same fundamental harmonic B_{gv} and k_{wv} (v=P_{PM}), but different modulated harmonics B_{gv} (v=$|P_{PM}$-$P_s|$) (Fig. 4(c)).

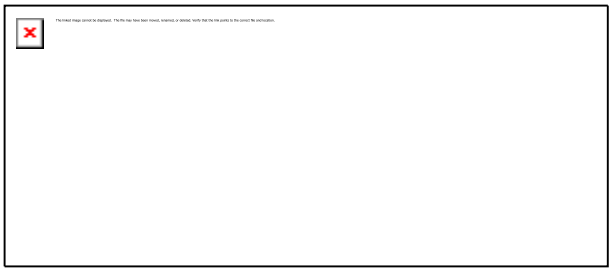

(a)

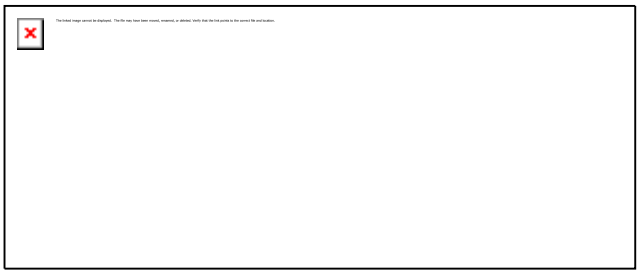

(b)

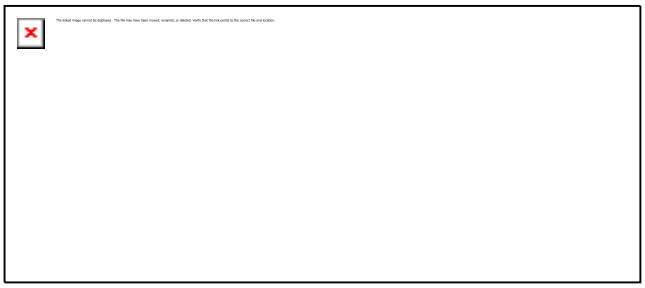

(c)

Fig. 4 Open-circuit PM flux density distributions with the same 24s. (a) 24s/8p and 24s/16p. (b) 24s/10p and 24s/14p. (c) 24s/11p and 24s/13p.

For the RPM-FS machines with different P_s but the same k_w, e.g., 12s/4p versus 24s/8p, the open-circuit air-gap flux density harmonic distributions are shown in Fig. 5. From Fig. 5(a), the amplitudes of fundamental harmonics with P_{PM} order and modulation harmonics $|P_{PM}\pm P_s|$ of the 24s/8p machine are higher than those of the 12s/4p machine due to the larger F_{RPMb}, as shown in Fig. 3. Similarly, the fundamental harmonic P_{PM} and modulation harmonics $|P_{PM}\pm P_s|$ of the 24s/10p and 24s/14p machines are higher than those of the 12s/5p and 12s/7p machines, respectively. Thus, it can be concluded that compared to the P_s=12 machines, the P_s=24 RPM-FS machines may exhibit larger B_{gv} (v=P_{PM}), which is helpful to select the attractive P_s/P_r combinations of the RPM-FS machines with different P_s but the same k_w.

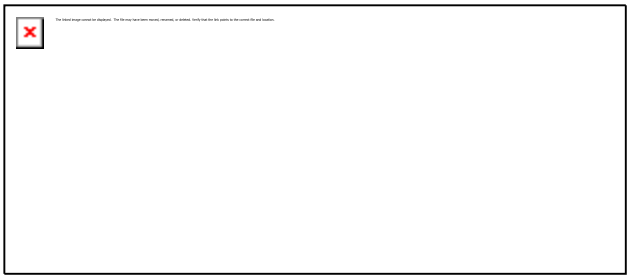

(a)

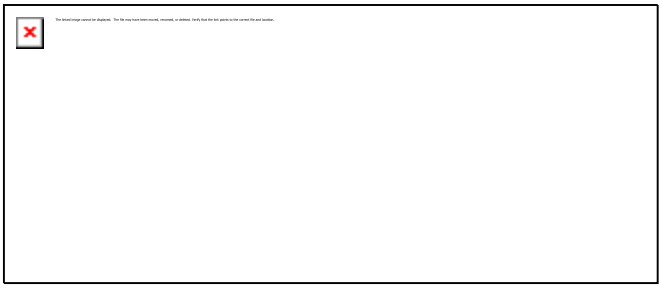

(b)

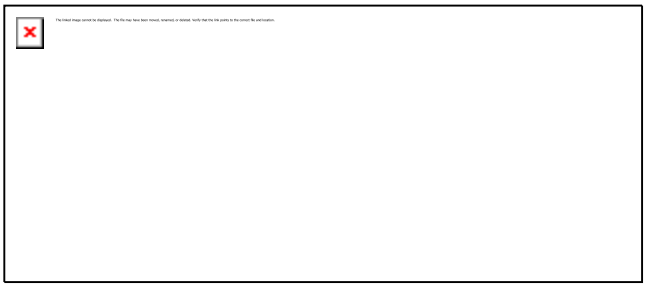

(c)

Fig. 5 Open-circuit air-gap flux density distributions with the same k_w. (a) 12s/4p and 24s/8p. (c) 12s/5p and 24s/10p. (d) 12s/7p and 24s/14p.

From equation (3), the PM air gap flux density harmonics rotation speed relative to the stator and rotor are listed in Table VI. The iron losses in RPM-FS machines with different P_s/P_r combinations are produced by the harmonics with the rotation speed $\omega_{rv}\neq 0$. For the stator parts, all harmonics rotation speeds relative to the stator are not zero in the PM air gap field. Hence, these harmonics generate iron losses in the stator cores. However, the rotation speed relative to the rotor of harmonics with nP_{PM} orders are zero, whereas the harmonics with $|nP_{PM}\pm kP_s|$ orders are not equal to zero. Hence, the iron losses in the rotor cores are generated by the modulation harmonic components, i.e., $|nP_{PM}\pm kP_s|$ orders.

In addition, the PMs are mounted in the rotor, then the PM eddy current loss P_{PMloss} is dominantly produced by the air gap filed harmonics, of which the rotation speeds relative to the rotor are not zero. Thus, the P_{PMloss} is produced by the harmonics with $|nP_{PM}\pm kP_s|$ orders.

Table VI

The Harmonic Components of PM Field Flux Density

Pole Pairs	Relative to stator Rotation speed	Relative to rotor Rotation speed
nP_{PM}	ω_r	0
$nP_{PM}+kP_s$	$nP_{PM}\omega_r/(nP_{PM}+kP_s)$	$kP_s\omega_r/(nP_{PM}+kP_s)$
$\|nP_{PM}-kP_s\|$	$nP_{PM}\omega_r/(nP_{PM}-kP_s)$	$kP_s\omega_r/(nP_{PM}-kP_s)$

2. Electrical loading

The v-order harmonic amplitude of electrical loading K_{sv} can be expressed as [11], [12]:

(7)

where J_{sa_rms} is the armature current density; and A_{slot} is armature slot area per phase. It is found that the fundamental harmonic of K_{sv} (v=P_{PM}) is only determined by the k_{wv} (v=P_{PM}) in the primitive design, since J_{sa_rms}=5A/mm^2 and A_{slot}=74mm^2 are constant values with different P_s.

Considering the salient stator and rotor cores, the armature reaction field is modulated by the salient teeth. Then, the electrical loading $K_s(\vartheta, t)$ yields [13] [14],

(8)

where M[.] is the modulation operator of salient teeth, $F_{Rw}(\vartheta, t)$ is armature reaction-MMF function, and $B_{Rw}(\vartheta, t)$ is modulated armature reaction air-gap flux density function. Then, the v-order harmonic amplitude K_{sv} is proportional to the harmonic amplitude vB_{Rwv}, i.e., K_{sv} vB_{Rwv}, which is analysed below.

For the 24s/10p machine, the modulated armature reaction flux density in the primitive design can be expressed as [12]:

(9)

where N_{Rc} is coil turns number; I_{Rmax} is the maximum value of the phase current; D_{Ri} is the Fourier coefficients of the armature reaction MMF; Λ_{Rr0}, Λ_{Rrb} and Λ_{Rrp} are the Fourier coefficients of rotor air-gap permeance; and p is 1, 2, 3…

(10)

(11)

The ξ, β_1 and β_2 can be expressed as follows:

(12)

(13)

According to equation (9), it can be found that certain harmonic components are generated in two ways, namely, fundamental components with (4i-2) orders are produced by the armature reaction MMF only and the resultant components with (pP_r±(4i-2)) orders are due to the salient rotor modulation effect, as shown in Table VII. For the harmonic with 14-orders, the fundamental component (4i-2)-orders (i=4) and resultant part |pP_r-(4i-2)| order (i=9, p=2) are the positive values, and the harmonic amplitude with 14-pole-pairs is superimposed by the two components. Similarly, the harmonics with 34-orders are heightened else. However, the amplitude of the 38-order harmonic is cancelled because the fundamental component and resultant part are opposite. Hence, the 38th harmonic order is significantly lower than 14th and 34th harmonics, which is verified in Fig. 7.

Table VII

The Harmonic Components of 24s/10p RPM-FS Machines

Harmonics	Fundamental components	Resultant components
v=14th	 (i=4)	 (i=9, p=2)
v=34th	 (i=9)	 (i=4, p=2)
v=38th	 (i=10)	 (i=15, p=2)

Table VIII

The Harmonic Components of 24s/14p RPM-FS Machines

Harmonics	Fundamental components	Resultant components

10th		
	(*i*=3)	(*i*=10, *p*=2)
34th		
	(*i*=9)	(*i*=16, *p*=2)
38th		
	(*i*=10)	(*i*=15, *p*=2)

For the 24s/14p RPM-FS machine, the winding function is similar to the 24s/10p RPM-FS machine, resulting in the same armature reaction MMF distribution between two machines, as shown in Fig. 6. Considering the salient iron core, the armature reaction air-gap flux-density harmonic distribution is shown in Fig. 7. It can be found from Table VIII that the harmonic amplitudes with 10- and 38-orders are enlarged by the fundamental and resultant parts, whereas 34-order is cancelled. In addition, the modulation harmonics of electrical loading K_{sv} (v=P_s±P_r) are mainly determined by the parameter vB_{Rwv}. For P_r=10 RPM-FS machine, vB_{Rwv}=2.24T (v=|P_s-P_r|) is higher, whereas vB_{Rwv}=1.88T (v=P_s+P_r) is lower than the case of P_r=14 (vB_{Rwv}=1.93T, v=|P_s-P_r| and vB_{Rwv}=2.77T, v=P_s+P_r). The modulation torque components are influenced further in Part D.

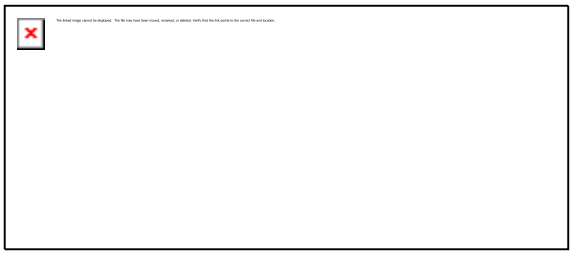

Fig. 6 Armature reaction MMFs of the 24s/10p and 24s/14p machines.

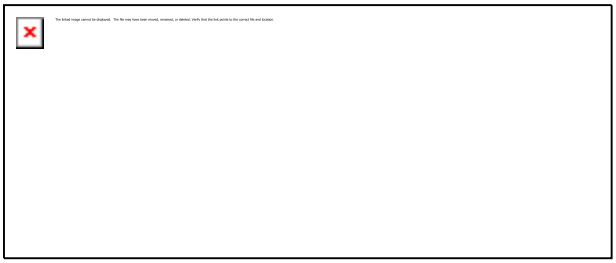

Fig. 7 Modulated armature reaction flux density in air-gap of the 24s/10p and 24s/14p machines.

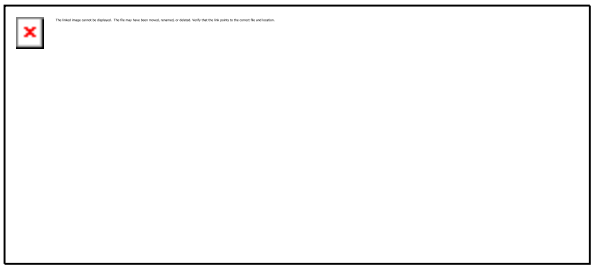

Fig. 8 Armature reaction MMFs of the 24s/11p and 24s/13p machines.

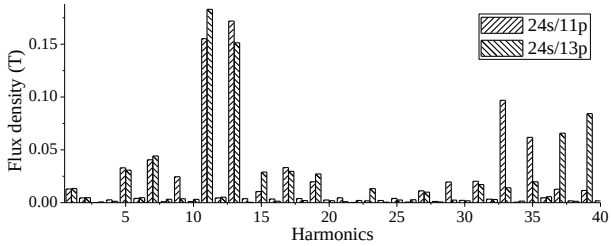

Fig. 9 Modulated armature reaction flux density in air-gap of the 24s/11p and 24s/13p machines.

The 24s/11p and 24s/13p RPM-FS machines also have the same winding function, and the armature reaction field harmonic distributions are the same as shown in Fig. 8. Taking the modulation effect due to salient teeth into consideration, the armature reaction air-gap flux density distributions are shown in Fig. 9. The 37-order harmonic in the P_r=11 machine and 35-order harmonic in the P_r=13 machine are weakened. In addition, the parameter vB_{Rwv}=2.43T (v=P_s+P_r=37th) in the P_r=13 machine is higher, whereas the vB_{Rwv}=2.01T (v=|P_s-P_r|=11) is lower than that of the P_r=11 machine (vB_{Rwv}=2.16T, v=35th and vB_{Rwv}=2.23T, v=13th), which results in a larger modulation torque in Part D.

From equation (9), the harmonic components of the armature reaction air gap flux density are listed in Table IX. For the stator parts, all harmonic components of the armature reaction flux density contribute to stator core loss because the effective harmonics rotation speed relative to the stator is not zero. However, for the rotor of the RPM-FS machine, if the harmonics satisfy equation (14), the rotation speed relative to the rotor is not equal to zero. Hence, the rotor core loss and P_{PMloss} are mainly contributed by these harmonic components in armature reaction flux density.

$$\begin{cases} HC \neq 4i-2, i=3 \\ HC \neq 4i-2 \pm pP_r, i=3 \end{cases} \quad (14)$$

Table IX

Harmonic Components of Armature Reaction Field Flux Density.

i	Pole Pairs	Relative to stator Rotation speed	Relative to rotor Rotation speed
	$4i$-2	$-P_r\omega_r/(4i\text{-}2)$	$(4i\text{-}2\text{-}P_r)\omega_r/(4i\text{-}2)$
i=3r-2	$4i$-2+pP_r	$(p\text{-}1)P_r\omega_r/(pP_r\text{+}4i\text{-}2)$	$(4i\text{-}2\text{+}P_r)\omega_r/(pP_r\text{+}4i\text{-}2)$
	$\lvert 4i\text{-}2\text{-}pP_r\rvert$	$(p\text{+}1)P_r\omega_r/[pP_r\text{-}(4i\text{-}2)]$	$-(4i\text{-}2\text{+}P_r)\omega_r/[pP_r\text{-}(4i\text{-}2)]$
	$4i$-2	$P_r\omega_r/(4i\text{-}2)$	$(4i\text{-}2\text{+}P_r)\omega_r/(4i\text{-}2)$
i=3r	$4i$-2+pP_r	$(p\text{+}1)P_r\omega_r/(pP_r\text{+}4i\text{-}2)$	$(4i\text{-}2\text{-}P_r)\omega_r/(pP_r\text{+}4i\text{-}2)$
	$\lvert 4i\text{-}2\text{-}pP_r\rvert$	$(p\text{-}1)P_r\omega_r/[pP_r\text{-}(4i\text{-}2)]$	$-(4i\text{-}2\text{-}P_r)\omega_r/[pP_r\text{-}(4i\text{-}2)]$

3. Cogging torque production

The torque ripple of the RPM-FS machine is dominantly influenced by the cogging torque [12], which is considered in the preliminary design process. The cogging torque can be expressed as [15], [16]:

$$T_{cog}(\theta_r) = -\frac{\partial W(\theta_r)}{\partial \theta_r} \tag{15}$$

where ϑ_r is the rotor rotation angle, $\vartheta_r=\omega_r t$, and ω_r is rotor mechanical angular velocity. $W(\vartheta_r)$ is magnetic energy, which can be expressed as:

$$W(\theta_r) = \frac{1}{16\mu_0}(D_{so}^2 - D_{si}^2) l_a \int_0^{2\pi} F_{RPM}^2(\theta,\theta_r)\Lambda_s^2(\theta)d\theta \tag{16}$$

where D_{so} and D_{si} are the outside and inside stator diameters, l_a is the stack length, μ_0 is air magnetic permeability, and $F_{RPM}^2(\vartheta, \vartheta_r)$ and $\Lambda_s^2(\vartheta)$ are the PM-MMF function and stator air-gap permeance function, respectively.

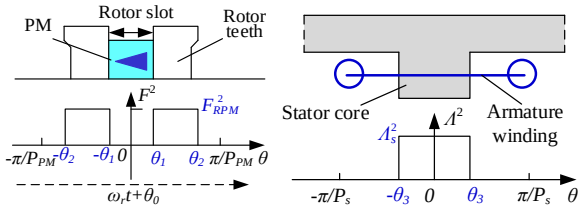

Fig. 10 PM-MMF-permeance model of RPM-FS machine.

Based on the PM-MMF permeance model shown in Fig. 10, the $F_{RPM}^2(\vartheta, \vartheta_r)$ can be expressed as:

$$F_{RPM}^2(\theta,\theta_r) = F_{RPM0} + \sum_{n=1}^{\infty} F_{RPMn}\cos[nP_{PM}(\theta+\theta_r)] \tag{17}$$

where P_{PM} is PM pole pairs, which is equal to rotor pole pairs P_r; n is 1, 2, 3…; and F_{RPM0} and F_{RPMn} are the Fourier coefficients.

The stator air-gap permeance $\Lambda_s^2(\vartheta)$ can be expressed as:

$$\Lambda_s^2(\theta) = \Lambda_{s0} + \sum_{k=1}^{\infty} \Lambda_{sk}\cos(kP_s\theta) \tag{18}$$

where P_s is stator teeth number, Λ_{s0} and Λ_{sk} are the Fourier coefficients, and k is 1, 2, 3…

Substituting equations (17) and (18) into equation (16), the magnetic energy $W(\vartheta_r)$ can be determined as:

$$W(\theta_r) = \frac{1}{16\mu_0}(D_{so}^2 - D_{si}^2) l_a [2\pi F_{RPM0}\Lambda_{s0} + \sum_{n=1}^{\infty}\sum_{k=1}^{\infty} F_{RPMn}\Lambda_{sk}\pi\cos(nP_{PM}\theta_r)] \tag{19}$$

where the nP_{PM} and kP_s are identical to avoid $W(\vartheta_r)$=0, i.e.,

$$nP_{PM}=kP_s=j\text{LCM}(P_s, P_{PM}),\ j=1, 2, 3\ldots \tag{20}$$

where the LCM(P_s, P_{PM}) is the lowest comment multiple of P_s and P_{PM}.

Hence, the cogging torque can be obtained as follows:

$$T_{cog}(\theta_r) = \frac{1}{16\mu_0}(D_{so}^2 - D_{si}^2) l_a \sum_{n=1}^{\infty}\sum_{k=1}^{\infty} F_{RPMn}\Lambda_{sk} nP_{PM}\pi\sin(nP_{PM}\theta_r) \tag{21}$$

It is found that the period of cogging C_{cog} is obtained as:

$$C_{cog} = \frac{2\pi}{nP_{PM}} = \frac{2\pi}{LCM(P_s, P_{PM})} \tag{22}$$

From equation (21), the amplitude of cogging torque can be calculated as

$$T_{cog} = \frac{(D_{so}^2 - D_{si}^2) l_a}{4\pi\mu_0} F_{RPM}^2 \Lambda_s^2 \frac{P_s}{n} \tag{23}$$

Since the parameters D_{so}, D_{si} and l_a are the constant values, as listed in Table V. Then, the T_{cog} is dominantly determined by

$$\frac{P_s}{n} = \frac{P_s P_{PM}}{LCM(P_s, P_{PM})} = GCD(P_s, P_{PM}) \tag{24}$$

It can be concluded that the appropriate P_s/P_{PM} combinations with lower cogging torque can be chosen by a lower GCD(P_s, P_{PM}) during the preliminary design.

For the RPM-FS machines (D_{si}=79.36mm) with the same stator teeth number, e.g., P_s=24, the cogging torques are listed in Table X. Then, according to equation (24), the P_r=8 and 16 machines exhibit higher cogging torques, whereas the P_r=11 and 13 machines obtain lower values. In addition, although the 8 and 16 pole pairs machines have the same GCD(P_s, P_{PM})=4, the former exhibits a lower cogging torque due to the smaller F_{RPMb} as shown in Fig. 3.

Table X

The cogging torque of different P_s/P_r combinations at P_s=24.

P_r	8	10	11	13	14	16
GCD(P_s, P_{PM})	8	2	1	1	2	8
T_{cog} (Nm)	1.4	0.9	0.12	0.12	0.8	4.6

4. Electromagnetic torque production

The electromagnetic torque T_e with different P_s/P_r are shown in Fig. 11. It can be found that T_e of RPM-FS machines are dominantly contributed by fundamental harmonic components with the P_{PM}-order, which is produced from the interaction between magnetic loading B_{gv} and electrical loading K_{sv} (v=P_{PM}) in equation (2). In addition, the fundamental harmonic of electrical loading K_{sv} is only influenced by k_{wv} (v=P_{PM}). Hence, the torque capability of machines with different P_s/P_r combinations are investigated using parameters B_{gv} and k_{wv}.

For the RPM-FS machine with the same P_s and k_{wv} (v=P_{PM}), e.g., 24s/8p versus 24s/16p in Fig. 11(a), T_e of the P_r=16 machine is 12.86 Nm, which is larger than the P_r=8 machine (10.81 Nm), due to the larger fundamental harmonic magnetic loading in the P_r=16 machine shown in Fig. 4(a). Similarly, from Fig. 11, higher T_e of RPM-FS machines with the same P_s and k_{wv} (v=P_{PM}) can be obtained by choosing a larger P_r.

However, compared to the 24s/10p and 24s/14p RPM-FS machines with the same P_s and k_{wv} (v=P_{PM}), the fundamental torque component T_{ef} contributed by the fundamental harmonic (v=P_{PM}) of two machines are approximately equal to 11.5 Nm in Fig. 12(a) since the corresponding fundamental B_{gv} and K_{sv} of the two machines are identical to those analysed above. However, for the modulation harmonic torque T_{em} produced by the modulation harmonic (v=|P_{PM}-P_s|), the 14-order in P_r=10 machine contributes -1.35 Nm, which is higher than that of the 10th harmonic in the P_r=14 machine (-1.1 Nm). This is attributed to the higher modulation of the harmonic amplitude of PM flux density B_{gv} and electrical loading K_{sv} (v=|P_{PM}-P_s|) in the P_r=10 machine. On the other hand, for the modulation harmonic torque T_{em} produced by the modulation harmonic (v=P_{PM}+P_s), the torque produced by the 34-order harmonic in the P_r=10 machine (2.55 Nm) is lower than that of the 38-order in P_r=14 machine (3.04 Nm). This is because the electrical loading K_{sv} (v=|P_{PM}+P_s|) in the P_r=10 machine is lower, and the corresponding magnetic loading harmonics with the |P_{PM}+P_s| order of both machines are approximately identical. Hence, the total electromagnetic torque T_e of the P_r=14 machine (13.5 Nm) is larger than that of the P_r=10 machine (12.7 Nm).

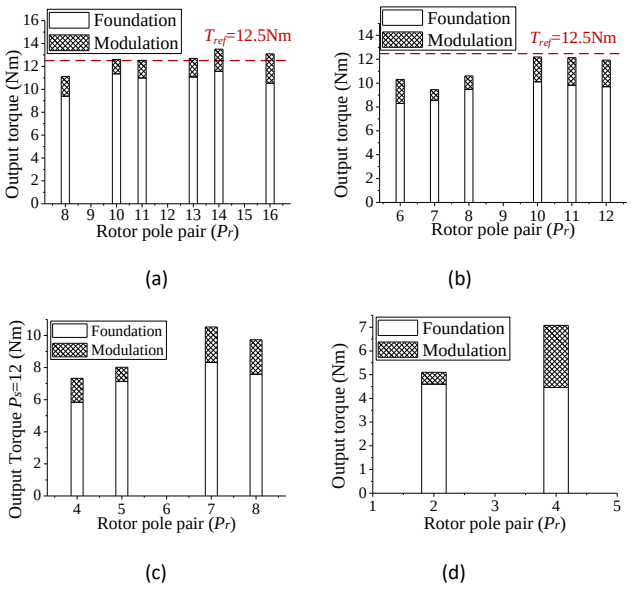

Fig. 11 The output torque with different P_s/P_r combinations of RPM-FS machines. (a) P_s=24. (b) P_s=18. (c) P_s=12. (d) P_s=6.

Similarly, the 24s/11p and 24s/13p RPM-FS machines also exhibit the same fundamental torque T_{ef}=11 Nm (v=P_{PM}), while the superimposed modulation torque T_{em} by v=|P_{PM}±P_s| order harmonics in the P_r=13 machine (1.62N m) is higher than that of the P_r=11 machine (1.44 Nm), as shown in Fig. 12(b) (v=|P_{PM}±P_s|). Finally, a

larger T_e=12.6 Nm is obtained in the P_r=13 machine. Therefore, it can be concluded that for the RPM-FS machines with the same fundamental magnetic loading B_{gv} and winding factor k_{wv} (v=P_{PM}), the fundamental harmonic contribution of electromagnetic torque are approximately equal, then the torque difference between RPM-FS machines is dominantly determined by the modulation harmonic torque components.

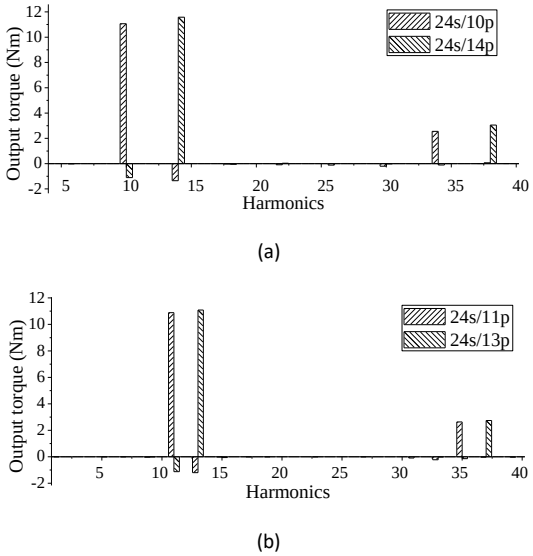

Fig. 12 Torque decompositions of the RPM-FS machine. (a) 24s/10p and 24s/14p. (b) 24s/11p and 24s/13p.

For RPM-FS machines with the same P_s but different k_{wv} (v=P_{PM}), e.g., the 24s/14p versus the 24s/16p in Fig. 11(a), a higher fundamental harmonic component of B_{gv} and k_{wv} (v=P_{PM}) in 14-pole-pairs machine results in a larger torque capability. T_e of the P_r=8 machine is the lowest among the candidates with P_s=24, due to the lowest B_{gv} and k_{wv} (v=P_{PM}). Similarly, for the machines with P_s=12 and 18 in Figs. 11(b) and (c), the highest T_e are obtained in the cases of 12s/7p and 18s/10p.

For the RPM-FS machines with different P_s but the same k_{wv} (v=P_{PM}), e.g., 12s/4p and 24s/8p with the same k_{wv}=0.866, it is found from Figs. 11(a) and (c) that T_e of the 12s/4p machine is 7.34 Nm, which is 68% of the 24s/8p machine, due to the larger fundamental harmonic of PM flux density in Fig. 5(a). Similarly, for the 12s/5p machine (k_{wv}=0.966), T_e is 8.02 Nm, which is 65% of the 24s/10p machine. In addition, T_e of the 12s/7p machine is 10.52 Nm, which is 78% of the 24s/14p machine.

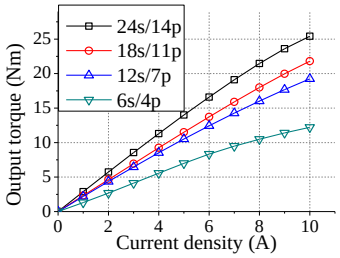

Fig. 13 The output torque of four RPM-FS machines versus different current densities.

To investigate the influence of overload capability by the P_s/P_r combinations, the 24s/14p RPM-FS machines is chosen, since this machine has a smaller rotor teeth width (θ_{rt}=π/(2P_r)), and exhibits a higher output torque at the P_s=24 condition. Similarly, the 6s/4p, 12s/7p and 18s/11p RPM-FS machines are also selected. It can be found from Fig. 13 that the output torque of RPM-FS machines increases linearly as the current density rises, and then all four machines exhibit satisfactorily overload capability. Therefore, the overload capability is hardly influenced by the P_s/P_r combinations of RPM-FS machines.

Based on the above analysis, the fundamental harmonics of magnetic loading B_{gv} and the winding factor k_{wv} (v=P_{PM}) are the key parameters to determine torque capability, where B_{gv} is mainly determined from the PM-MMF amplitude F_{RPMb} in equation (3). Therefore, based on the analysis of F_{RPMb} and k_{wv} in Fig. 3 and Tables I-IV, the attractive combinations of P_s/P_r of RPM-FS machines are chosen as follows.

(1) Feasible P_s/P_r combinations can be deduced based on the slot-conductor back-EMF star vector theory; meanwhile, the fundamental winding factor k_{wv} (v=P_{PM}) is calculated.

(2) The optimal range of P_r can be determined through the analysis of PM-MMF. Since the base speed in this paper is only 1500 r/min, a higher P_r can be selected to obtain larger magnetic loading B_{gv} (v=P_{PM}), i.e., 10<P_r<20.

(3) The attractive P_s=18 and 24 are selected since the counterparts with low P_s and high P_r (e.g., 12s/16p, 6s/10p and 6s/14p machines) cannot exhibit the flux-switching principle, which results in a lower torque capability.

(4) Considering k_{wv} (v=P_{PM}), the candidates of RPM-FS machines with 18s/10p, 18s/11p, 18s/12p, 24s/10p, 24s/11p, 24s/13p, 24s/14p and 24s/16p are chosen, which is highlighted in Tables I-IV.

(5) The P_s/P_r combinations with lower cogging torque can be chosen based on a smaller GCD(P_s, P_{PM}), which may result in small torque ripple for the RPM-FS machines. Thus, the 18s/12p and 24s/16p RPM-FS machines are removed.

The candidates chosen by F_{RPMb} and k_{wv} at preliminary design exhibits higher torque capability, which is verified in Fig. 11. Then, by considering the GCD(P_s, P_{PM}), the P_s/P_r combinations with lower cogging torque are obtained. To reduce the candidates further, the reference torque is set to be 12.5 Nm, which is equal to the output torque of the 12s/10p SPM-FS machine in the preliminary design. Consequently, T_e of the 24s/10p, 24s/11p, 24s/13p and 24s/14p RPM-FS machines in the primitive design are larger than the reference torque 12.5 Nm, these are selected and analysed further.

3. Performance Comparison and Verification

To verify the feasibility of above P_s/P_r combination principle, a torque performance comparison between four RPM-FS machines candidates with 24s/10p, 24s/11p, 24s/13p and 24s/14p, together with a 12s/10p SPM-FS machine is conducted. The key parameters of five machines are listed in Table XI, where each machine is pre-optimized under the identical stator outside diameter, stack length and air-gap length for a fair comparison. Furthermore, the armature winding current densities and DC-bus voltages are the same, i.e., J_{sa_rms}=5 A/mm^2 and U_{dc}=600 V. The PM operation temperature is 90°C.

1. Electromagnetic Torque

The cogging torque waveforms of the five machines are shown in Fig. 14(a). The 12s/10p SPM-FS machine exhibits the highest peak-to-peak value of cogging torque (3.4 Nm), which results in the largest torque ripple in Fig. 14(b). For the RPM-FS machines, the 24s/11p and 24s/13p machines have smaller cogging torques (0.2 Nm), which is approximately 15% and 40% of those with 10- and 14-rotor-pole-pairs, respectively.

Fig. 15(a) shows the output torque of five machines with different current densities. Since the dq-axes inductances are nearly identical, the i_d=0 control is utilized in the five machines. It is found that the output torques of the four RPM-FS machines are always larger than the SPM-FS machine, which verifies that the RPM-FS machines have better torque capability. The output torque of the 24s/10p RPM-FS machine is 16.05 Nm at J_{sa_rms}=5 A/mm^2, which is 1.08 times that of the 12s/10p SPM-FS machine. Obviously, the average torque of the 24s/14p machine reaches a maximum value of 17.6 Nm at rated current density of 5 A/mm^2, which is 1.09 times, 1.11 times and 1.03 times that of the P_r=10, 11 and 13 RPM-FS counterparts. In addition, the masses of magnetic material and the PM utilization ratios $k_{T/MPM}$ (the ratio of the average torque to the PM mass) are listed in Table XI. It can be found that $k_{T/MPM}$ of the SPM-FS machine is only 16.4 Nm/kg, which is significantly lower than the four RPM-FS machines. The core losses and PM losses are listed in Table XI, where the core losses are analyzed based on the improved Yamazaki's model [17, 18], and the PM eddy current losses are calculated by the 3D-FEA. The predicted efficiencies of two machines at rated operation point are almost same.

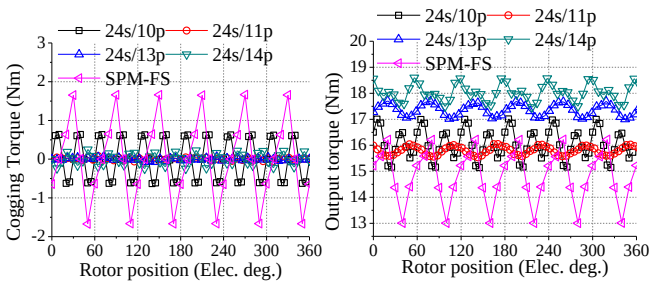

Fig. 14 The torque waveforms of RPM-FS machines and SPM-FS machine. (a) Cogging torque waveforms. (b) Output torque waveforms.

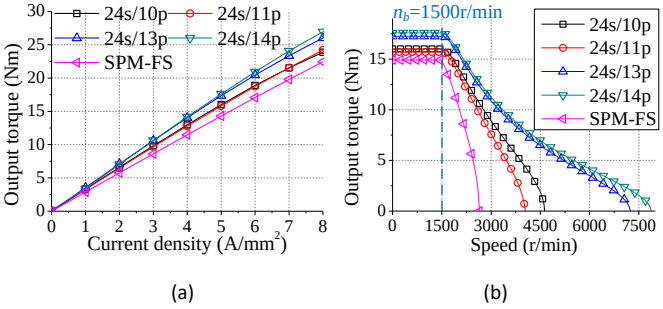

Fig. 15 The torque performances of four RPM-FS machines and the SPM-FS machine. (a) The output torque versus different current densities. (b) The output torque versus different speeds.

Table XI

The Optimal Dimensions and Performances of Five Machines

Key Parameters	RPM-FS (P_s=24)				SPM-FS
	P_r=10	P_r=11	P_r=13	P_r=14	12s/10p
D_{si} (mm)	76.80	79.36	76.80	79.36	70.4
D_{ro} (mm)	76.10	78.66	76.10	78.66	69.7
θ_{st} (deg.)	7.20	6.55	6.92	6.43	7.5
θ_{rt} (deg.)	9.90	8.18	7.62	7.07	10.5
θ_{rs} (deg.)	7.20	7.36	5.54	5.14	—
PM width w_{PM} (mm)	4.54	4.26	3.49	3.35	4.6
PM height h_{PM} (mm)	9.79	9.41	9.80	9.4	28.8
Phase turns N_p	264	268	240	228	280
R_{phase} (Ω) @25°C	1.2	1.24	0.94	0.89	1.9
Ψ_{PM} (Wb)	0.124	0.116	0.094	0.084	0.185
L_d (mH)	8.8	7.8	7.3	6.4	11.64
L_q (mH)	9.2	7.8	7.3	6.5	14.97
k_{fw}	2.47	2.23	3.8	4.03	1.51
Cogging (Nm)	1.4	0.2	0.2	0.5	3.4
T_e (Nm)	16.05	15.8	17.35	17.6	14.8
Torque ripple (%)	11%	3%	3%	6%	22%
Mass of PM (kg)	0.27	0.27	0.27	0.27	0.9
$k_{T/MPM}$ (Nm/kg)	59.4	58.5	64.3	65.1	16.4
Output power (W)	2521	2482	2725	2761	2324.6
Core loss (W)	60	53	65	69	51
Copper loss (W)	158.8	156.3	158	159.1	103.8
PM loss (W)	3.9	5.2	6.2	7.1	30.95
Efficiency (%)	90.2%	90.4%	90.6%	90.5%	90.9%
Power factor	0.89	0.88	0.85	0.83	0.91

2. Flux-Weakening Capacity

The flux-weakening capacity coefficient k_{fw} is another key parameter for evaluating the speed regulation range of traction machines for EV and HEV applications [19], [20]. expressed as:

(25)

where Ψ_{PM} is the peak value of PM flux linkage, and L_d and i_d are the d-axis inductance and armature current, respectively. Based on the PM flux-linkages, the d-axis inductances and the armature currents in Table XI, the flux-weakening coefficients k_{fw} of five machines can be calculated as listed in Table XI. Compared to the 12s/10p SPM-FS machine with the same structural dimensions, the four RPM-FS machines have a larger k_{fw} and exhibit a wider range of speed regulations under the same DC-bus voltage (600 V), as shown in Fig. 15(b). For the four RPM-FS machines, the maximum speed of the 24s/14p machine is 8000 r/min, which is higher than those with 24s/10p (4600 r/min), 24s/11p (3700 r/min) and 24s/13p (7200 r/min). In addition, the P_r=14 machine exhibit the lowest L_d and L_q among four RPM-FS machines, since the per phase turns N_p of P_r=14 machine is the smallest (N_p=228).

3. Experimental Verification

To validate the torque performances of the candidate RPM-FS machines, the prototypes of a 24s/10p RPM-FS machine and a 12s/10p SPM-FS machine were manufactured as shown in Fig. 16 [12]. Two machines are chosen with the same rotor-pole-pairs to maintain identical operation frequencies, and the main design parameters are in accordance with those listed in Table XI. The experiment platform is shown in Fig. 17(a). A DSP-TMS320F28335 based digital controller is designed to control the prototype machines. The field current is supplied by a DC power source. The variable load is a dynamometer, which is composed of an induction motor and a variable-frequency driver ABB-ACS800. The torque transducer HBM-T40 is mounted on the platform as shown in Fig. 17(a), which can be used to measure the transient torque values, and then the values can be displayed in a monitor of ABB-ACS800.

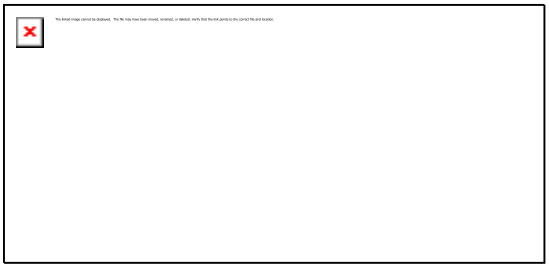

(a)

(b)

Fig. 16 The Prototype flux switching machines. (a) 24s/10p RPM-FS machine. (b) 12s/10p SPM-FS machine. [12]

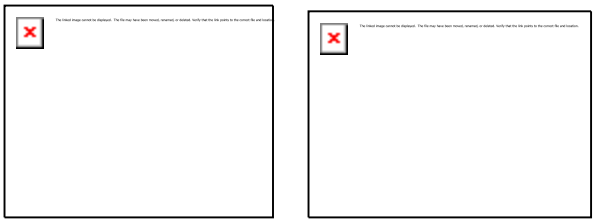

(a) (b)

Fig. 17 The experiment platforms of FS machines. (a) The output torque and power test platform. (b) The cogging torque test platform.

The 3D-FEA simulated and measured output torque of the 24s/10p RPM-FS machine is shown in Fig. 18, for which the rated speed is 1500 r/min [12]. It can be found that the measured output torque increases linearly as current density rises, which agrees well with the 3D-FEA results. The measured torque of RPM-FS machine at the rated current density of 5 A/mm^2 is 15 Nm, which is slightly lower than that of the 3D-FEA result. For the 12s/10p SPM-FS machine, the measured torque at J_{sa_rms}=5 A/mm^2 is 11.8 Nm, which is 95% of that of the 3D-FEA result. The error between measured and 3D-FEA results in the RPM-FS and SPM-FS machines can be attributed to different manufacturer tolerances. The power factors of two machines at rated torque and speed 1500 r/min are measured to be 0.88, which are slightly lower than the FEA results in Table XI. Furthermore, the armature windings temperature of RPM-FS machine and SPM-FS machine are measured at rated J_{sa_rms}=5A/mm^2, and the corresponding results are 110°C and 97°C, which verifies the rated torque and speed for continuous operation.

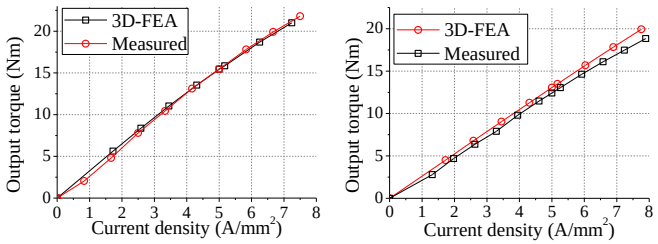

(a) (b)

Fig. 18 Measured and predicted output torque vs. current densities. (a) 24s/10p RPM-FS machine. (b) 12s/10p SPM-FS machine [12].

The cogging torque experiment platform is shown in Fig. 17(b). The cogging torque meter is mounted on the platform. The principal computer is utilized to collect data from cogging torque meter, and display the cogging torque waveforms. Then, the cogging torque of 24s/10p RPM-FS machine and 12s/10p SPM-FS machine are measured as shown in Fig. 19. It can be found that the measured cogging torque waveforms of two machines are approximately coincide well with the 3D-FEA results. The difference between experiments and 3D-FEA can be attributed to the prototypes manufacture tolerance and the inaccurate assembling process. The measured peak value of RPM-FS machine is 0.9Nm, which is significantly lower than that of SPM-FS machine (4Nm).

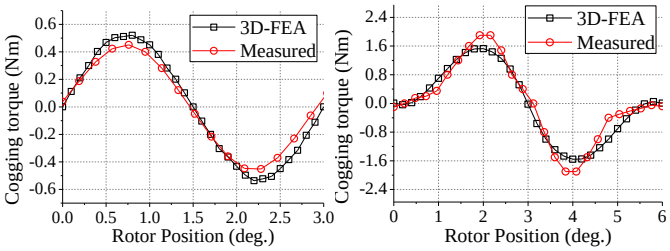

(a) (b)

Fig. 19 Measured and predicted cogging torque. (a) 24s/10p RPM-FS machine. (b) 12s/10p SPM-FS machine.

The output torque of 24s/10p RPM-FS machines and 12s/10p SPM-FS machine with different speed regulation ratios (the ratio of speed to base speed) are measured as shown in Fig. 20. It can be seen that the measured and 3D-FEA torque-speed waveforms are in good agreement. In the constant-torque region, the i_d=0 control is utilized and the q-axis RMS current density of two machines are J_{sa_rms}=5A/mm^2. It can be found that the output torque of RPM-FS machine is 15Nm, which is 1.25 times of that SPM-FS machine. In the flux weakening region, two machines are operated under the same DC bus voltage, i.e. 200V. It can be seen that the maximum speed regulation ratio of RPM-FS

machine is 3, which means 3 times of base speed can be obtained in RPM-FS machine with flux weakening control. For the SPM-FS machine, the maximum speed regulation ratio is only 1.8, and the flux weakening region is significantly narrow than the RPM-FS machine.

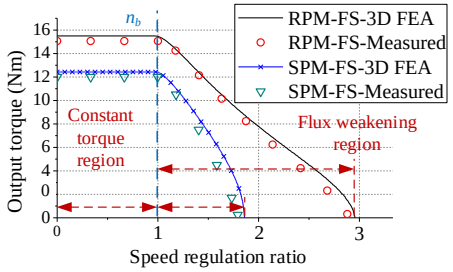

Fig. 20 The output torque versus different speed values of 24s/10p RPM-FS machines and 12s/10p SPM-FS machine.

The efficiency maps of 24s/10p RPM-FS machine and 12s/10p SPM-FS machine are shown in Fig. 21. It can be found that the measured operation points of two machines are slightly lower than the FEA results. For the rated operation point of RPM-FS machine (T_e=15Nm, n_b=1500r/min), the measured efficiency is 90.3%, which is approximately identical to that of the 3D-FEA result. For the SPM-FS machine, the measured rated operation point is T_e=11.8Nm and n_b=1500r/min. It can be found that a reduction of 0.3% of the measured efficiency (90.1%) is obtained compared with the 3D-FEA result.

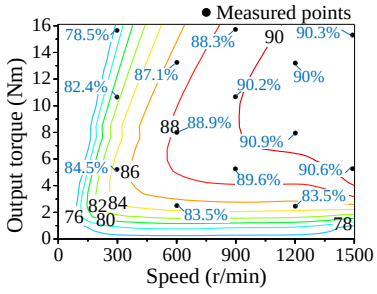

(a)

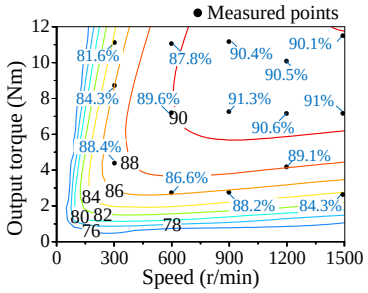

(b)

Fig. 21 The efficiency maps of two machines. (a) The RPM-FS machine. (b) The SPM-FS machine.

4. Conclusion

In this paper, the influence of P_s/P_r combinations on electromagnetic torque performances in RPM-FS machines is investigated, which is helpful to choose the candidates with higher torque capability. The conclusions are as follows:

(1) The electromagnetic torque T_e of RPM-FS machine is mainly (>80%) contributed by the fundamental harmonic torque, which is determined by the fundamental PM MMF and winding factor k_{sv} in the preliminary design.

(2) The attractive P_s/P_r combination candidates are changed at the different stator outer diameter D_{so}. Since the variation of PM MMF with P_r is influenced by the key parameter D_{so} based on the magnetic circuit analysis based on the magnetic circuit analysis.

(3) For the machines with the same fundamental PM MMF and k_{wv}, the fundamental harmonic contributions of electromagnetic torque are approximately identical, then the difference of T_e between RPM-FS machines is dominantly determined by the modulation harmonic torque components.

(4) Taking the cogging torque influence into consideration, the candidates exhibiting lower torque ripple can be obtained by lower GCD(P_s, P_r).

Based on the analysis of PM MMF, k_{wv} and GCD(P_s, P_r), the 24s/10p, 24s/11p, 24s/13p and 24s/14p RPM-FS machines are chosen to be the candidates at D_{so}=128mm. Compared with a typical 12s/10p SPM-FS machine with the same structure dimensions, these four RPM-FS machines exhibit higher torque capability and wider speed regulation range. The characteristics of P_s/P_r combinations are verified by the FEA and experiments. Therefore, employing the proposed techniques is helpful for choosing attractive P_s/P_r combinations promptly and effectively for certain space dimensions.

References

X. Zhu, Z. Xiang, C. Zhang, L. Quan, Y. Du, and W. Gu, "Co-reduction of torque ripple for outer rotor flux-switching PM motor using systematic multi-level design and control schemes", *IEEE Trans. Ind. Electro.*, vol. 64, no. 2, pp. 1102-1112, Feb. 2017.

C. Liu, "Emerging Electric Machines and Drives–An Overview." *IEEE Trans. Eng. Convers.* DOI: 10.1109/TEC.2018.2852732.

1. A. Fasolo, L. Alberti, N. Bianchi. "Performance comparison between switching-flux and IPM machines with rare-earth and ferrite PMs," *IEEE Trans Ind. Appl.*, vol. 50, no. 6, pp. 3708-3716, Nov./Dec., 2014.

T. Wang, C. Liu, W. Xu, G. Lei, M. Jafari, Y. Guo. "Fabrication and experimental analysis of an axially laminated flux switching permanent magnet machine." *IEEE Trans. Ind. Electro.*, vol. 64, no. 2, pp. 1081-1091, Feb. 2017.

2. P. Su, W. Hua, G. Zhang, Z. Chen, and M. Cheng. "Analysis and evaluation of novel rotor permanent magnet flux-switching machine for EV and HEV applications." *IET Electr. Power App.*, vol. 11, no. 9, pp. 1610-1618, Nov. 2017.

S. Jia, R. Qu, W. Kong, D. Li, J. Li, and R. Zhang. "Stator/rotor slot and winding pole pair combinations of DC biased current Vernier reluctance machines." *IEEE Trans. Ind. Appl.* vol. 54, no. 6, pp. 5967-5977, Jul. 2018.

3. Y. Shi, L. Jian, J. Wei, W. Li, and C. C. Chan. "A new perspective on the operating principle of flux-switching permanent magnet machines." *IEEE Trans. Ind. Electron.*, vol. 63, no. 3, pp. 1425-1437, Mar. 2016.
4. J. T. Chen, and Z.Q. Zhu. "Winding configurations and optimal stator and rotor pole combination of flux-switching PM brushless AC machines." *IEEE Trans. Energy Convers.*, vol. 25, no. 2, pp. 293-302, Jun. 2010.
5. J. D. McFarland, T. M. Jahns, and A. M. EL-Refaie. "Analysis of the torque production mechanism for flux-switching permanent-magnet machines." *IEEE Trans. on Ind. Appl.*, vol. 51, no. 4, pp. 3041-3049, Jul./Aug. 2015.
6. D. Li, R. Qu, J. Li, W. Xu, and L. Wu. "Synthesis of flux switching permanent magnet machines." *IEEE Trans. Energy Convers.*, vol. 31, no. 1, pp. 106-117, Mar. 2016.
7. N. Bianchi, M. D. Pre, L. Alberti, and E. Fornasiero. "Theory and design of fractional-slot PM machine." 1st ed. *CLEPU*, 2007.
8. P. Su, W. Hua, Z. Z. Wu, P. Han, M. Cheng. "Analysis of the operation principle for rotor permanent magnet flux switching machines." *IEEE Trans. Ind. Electro.*, vol. 65, no. 2, pp. 1062-1073, Feb. 2018.
9. M. Cheng, P. Han. "A General Airgap Field Modulation Theory for Electrical Machines." *IEEE Trans. Ind. Electro.*, vol. 64, no. 8, pp. 6063-6674, Aug. 2017.
10. Z. Z. Wu and Z. Q. Zhu. "Analysis of air-gap field modulation and magnetic gearing effects in switched flux permanent magnet machines." *IEEE Trans. Mag.*, vol. 51, no. 5, Art. No. 8105012, May. 2015.
11. Z.Q. Zhu, D. Howe. "Influence of design parameters on cogging torque in permanent magnet machines." *IEEE Trans. Energy Convers.*, vol. 15, no. 4, pp. 407-412, Dec. 2000.
12. C. Gan, J. Wu. "Investigation of short permanent magnet and stator flux bridge effects on cogging torque mitigation in FSPM machines." *IEEE Trans. Energy Convers.*, vol. 33, no. 2, pp. 845-855, Feb. 2018.
13. Yamazaki, K., "Torque and efficiency calculation of an interior permanent magnet motor considering harmonic iron losses of both the stator and rotor," *IEEE Trans. Magn.*, vol. 39, no. 3, pp. 1460-1463, May 2003.
14. Zhu, S., Cheng, M., Dong, J., Du, J., "Core loss analysis and calculation of stator permanent-magnet machine considering DC-biased magnetic induction," *IEEE Trans. Ind. Electron.*, vol. 61, no. 10, pp. 5203-5212, Oct. 2014.
15. W. Fei, P. Chi. "A novel permanent-magnet flux switching machine with an outer-rotor configuration for in-wheel light traction applications," *IEEE Trans Ind. Appl.*, vol. 59, no. 5, pp. 1496-1506, Sep./Oct., 2012.
16. X. Liu, H. Chen, J. Zhao and A. Belahcen, "Research on the performances and parameters of interior PMSM used for electric vehicles". *IEEE Trans. Ind. Electro.*, vol. 63, no. 6, pp. 3533-3545, Feb. 2016.

research interests include the design, analysis, and control of electrical machines.

Peng Su (S'14) was born in Henan, China, in 1988. He received the B.Sc. and M.E. degrees in electrical engineering from Henan Polytechnic University, Henan, China in 2011 and 2013, respectively. Since 2013, he is currently working toward the Ph.D. degree in electrical engineering at Southeast University, Nanjing, China. From December 2016 to December 2017, he was a joint Ph.D. student funded by China Scholarship Council in the Department of Energy Technology, Aalborg University, Aalborg, Denmark.

His current research interests include the design and analysis of novel permanent-magnet brushless electrical machines for application in electric vehicles.

Wei Hua (SM'16) was born in Taizhou, China, in 1978. He received the B.Sc. and Ph.D. degrees in electrical engineering from Southeast University, Nanjing, China, in 2001 and 2007, respectively.

From September 2004 to August 2005, he visited the department of Electronics and Electrical Engineering, The University of Sheffield, UK, as a Joint-Supervised Ph. D student. Since 2007, he has been with Southeast University, where he is currently a Professor with the School of Electrical Engineering. He is the author or coauthor of over 150 technical papers, and he is the holder of 50 patents in his areas of interest. His teaching and

Mingjin Hu received the B.Eng. degree in electrical engineering from the School of Electrical Engineering, Southeast University, Nanjing, China, 2016. Since 2016, he is currently working toward the M.E. degree in electrical engineering at Southeast University, Nanjing, China.

His current research interests include the modeling and advanced control of electrical machines.

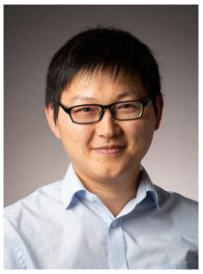

Zhongze Wu (S'15-M'18) received the B.Eng. and M.Sc. degrees in electrical engineering from the Chien-Shiung Wu College and the School of Electrical Engineering, Southeast University, Nanjing, China, in June 2010 and March 2013, respectively, and the Ph.D. degree in Electronic and Electrical Engineering from The University of Sheffield, Sheffield, U.K., in January 2017.

Since August 2018, he has been with Powertrain and Vehicle Research Centre, Department of Mechanical Engineering, University of Bath, Bath, U.K., where he is currently a Prize Fellow. His current research interests include the analysis, design, control and manufacturing of advanced machines and drives for electric propulsion systems.

From January 2017 to August 2018, he was with Warwick Manufacturing Group (WMG), University of Warwick, Coventry, U.K., as a research fellow.

Jikai Si received the B.S. degree in electrical engineering and automation from the Jiaozuo Institute of Technology, Jiaozuo, China, in 1998; the M.S. degree in electrical engineering from Henan Polytechnic University, Jiaozuo, China, in 2005; and the Ph.D. degree in electrical engineering from the School of Information and Electrical Engineering, China University of Mining and Technology, Xuzhou, China, in 2008. He is currently a distinguished professor at Zhengzhou University.

His main research interests include the theory, application, and control of special motor. He has authored and co-authored over 100 technical papers in these areas. Prof. Si is a Member of the Institute of Linear Electric Machine and Drives, Henan Province, China.

Zhe Chen (M'95–SM'98- F'18) received the B.Eng. and M.Sc. degrees all in electrical engineering from Northeast China Institute of Electric Power Engineering, Jilin City, China, in 1982 and 1986, respectively, the M.Phil. degree in power electronic from Staffordshire University, Staffordshire, U.K., in 1993, and the Ph.D. degree in power and control from University of Durham, Durham, U.K., in 1997.

He is a Full Professor with the Department of Energy Technology, Aalborg University, Aalborg, Denmark, since 2002. He is the Danish Principle Investigator for Wind Energy of Sino-Danish Centre for Education and Research and the leader of Wind Power System Research program at the Department of Energy Technology, Aalborg University. He has led many international and national research projects and has more than 500 technical publications with more than 12500 citations (Google Scholar) and h-index of 49. His research interests include power systems, power electronics, and electric machines; and his main current research interests are wind energy and modern power systems.

Dr. Chen is an Associate Editor of the IEEE TRANSACTIONS ON POWER ELECTRONICS, a Fellow of the Institution of Engineering and Technology, London, U.K., and a Chartered Engineer in the U.K.

Ming Cheng (M'01–SM'02–F'15) received the B.Sc. and M.Sc. degrees in Electrical Engineering from the Department of Electrical Engineering, Southeast University, Nanjing, China, in 1982 and 1987, respectively, and the Ph.D. degree in electrical engineering from the University of Hong Kong, Hong Kong, in 2001.

Since 1987, he has been with Southeast University, where he is currently a Distinguished Professor in the School of Electrical Engineering and the Director of the Research Center for Wind Power Generation. From January to April 2011, he was a Visiting Professor with the Wisconsin Electric Machine and Power Electronics Consortium, University of Wisconsin-Madison. His teaching and research interests include electrical machines, motor drives for electric vehicles, and renewable energy generation. He has authored or coauthored over 350 technical papers and 4 books and is the holder of 90 patents in these areas.

Prof. Cheng is a fellow of the Institution of Engineering and Technology. He has served as chair and organizing committee member for many international conferences. He is a Distinguished Lecturer of the IEEE Industry Applications Society (IAS) in 2015/2016.